ICAS 2021 SHANGHAI
International Council of the Aeronautical Sciences
32nd Congress of the International Council of the Aeronautical Sciences
September 6-10, 2021
Pudong Shangri-La, Shanghai, China

RESEARCH OF THE HYPERSONIC BOUNDARY LAYER INSTABILITIES AND TRANSITION WITH THERMAL-CHEMICAL NON-EQUILIBRIUM EFFECTS

Xianliang Chen & Song Fu

Tsinghua University, Beijing, 100084

Abstract

Compared to the widely-studied linear instabilities, the nonlinear analyses of the high-enthalpy and hypersonic boundary-layer transition had received much less attention. In this paper, the tools of the nonlinear parabolized stability equations (NPSE) and the Floquet analysis (or the secondary instability theory, SIT) methods are employed to study the two important transition mechanisms in the hypersonic and high-enthalpy boundary layers with thermal-chemical non-equilibrium effects, including the secondary instability of the axisymmetric second-mode wave and the second-mode oblique-wave breakdown. The case studied is the flow over a blunt cone with the free-stream Mach-number of 15 and zero angle-of-attack. The fundamental resonance is found to dominate over the subharmonic resonance. Taking advantage of the high efficiency of SIT, the optimal azimuthal wavenumber is determined corresponding to the strongest secondary growth. For the fundamental resonance, the effects of TCNE on the secondary instability are found similar to increase the primary wave amplitude that leads to a higher maximum secondary growth rate and the corresponding azimuthal wavenumber. For the oblique-mode breakdown, the higher growth rate of the second-mode waves leads to faster growth of the streamwise vortex and other harmonic waves.

Keywords: hypersonics, transition, thermal-chemical non-equilibrium

1. Introduction

The accurate prediction and effective control of the hypersonic boundary layer transition are especially helpful in designing thermal protection systems and engine intake for high-speed vehicles. However, the transition process is extremely complicated, mainly because of its high nonlinearity and sensitivity to many factors [1]. The flow transition is even more complicated in high-enthalpy boundary layers with the appearance of "high-temperature (real-gas) effects" [2]. Specifically, high temperature excites the vibrational and electronic energies in molecules, as well as causes chemical dissociation and even ionization, which invalidates the calorically perfect gas (CPG) assumption. It is a question of how high-temperature affects the boundary layer transition process.

In flight where the free stream is usually "quiet", the natural transition is a more likely route [3]. Here the disturbance within the boundary layer is excited through receptivity mechanisms, experiences linear amplification, and then parametric resonance before the final breakdown to turbulence. From the linear stability theory (LST) [4], it is known that the second-mode instability becomes dominant when the free-stream Mach number is over 4. When the most unstable two-dimensional second-mode wave is linearly amplified to sufficiently high amplitude, nonlinear interaction comes into play leading to the rapid growth of three-dimensional waves. Here the large amplitude two-dimensional wave is referred to as the primary instability wave, in contrast to the three-dimensional one as the secondary instability wave. According to the frequency relation between the primary and secondary waves, the resonance mechanisms are divided into three types, namely fundamental, subharmonic and detuned resonance [5]. Besides, the oblique breakdown is also a viable path to turbulence with initially only a pair of oblique waves [6]. For the numerical study of these nonlinear processes, a series of numerical techniques were established, including direct numerical simulations (DNS) [6],

parabolized stability equations (NPSE) [7], and secondary instability theory (SIT) [5]. Researchers using these techniques emphasized the important role of the fundamental resonance [8] and oblique breakdown [7] concerning the second-mode wave for hypersonic boundary layers. Besides, the mechanism of the detuned resonance was highlighted where the low-frequency first mode and Görtler mode were heavily amplified through the interaction with the second mode [9].

For high-enthalpy boundary layers, physical models and numerical methods for laminar flow solutions were primarily established. When the time scales of these thermal-chemical processes are comparable to that of the flow, finite-rate models of the energy relaxation and chemical reactions are required to simulate the thermal-chemical non-equilibrium (TCNE) flow [10]. Based on these TCNE models, linear instability characteristics were widely studied for high-enthalpy boundary layers. Results showed that the first mode was more stable and the second mode was destabilized as the boundary layer became cooler and thinner. Meanwhile, energy relaxation and chemical endothermic reactions absorbed the disturbance energy to stabilize the modal growth [11]. The separate effects of these two paths were reflected by the dimensionless Damköhler number (the ratio of the thermal/chemical time scale to the flow time scale). Based on the linear instability results, the e^N method can be used to predict the transition onset. In contrast, the nonlinear stage of the disturbance evolution received little attention in high enthalpy boundary layers. Marxen et al. [12] simulated the fundamental resonance in the case of a Mach-10 adiabatic flat plate. They concluded that chemical reactions didn't directly influence the secondary growth but indirectly affected the change of the primary instability. Nevertheless, the selecting mechanisms in the parametric resonance require further investigation to find the dominant one. Also, the applicability of the Floquet theory for the secondary instability analysis is not clear. In addition, the oblique-mode breakdown process with high-temperature effects hasn't been investigated yet. Its transition mechanism and characteristic flow structures need to be explored. This paper aims to develop the nonlinear PSE and Floquet analysis methods for thermal-chemical non-equilibrium flows. The selected case is the flow over a blunt cone with the free-stream Mach number of 15. The two important transition mechanisms are separately studied, including the secondary instability of the axisymmetric second-mode wave and the second-mode oblique-wave breakdown.

2. Physical models and numerical methods

2.1 Governing equations

At the temperature lower than 9000 K, electronic processes are usually negligible. The five species model of air (N_2, O_2, NO, N, O) is selected. Extra conservations of species mass and vibrational energy are added to the governing equation as compared with that for CPG flows. The physical models adopted for TCNE flows follow the authors' previous works [13, 14]. The N-S equation is written in an operator form as

$$\mathcal{L}(\boldsymbol{q}) = \mathbf{S}(\boldsymbol{q}) \tag{1}$$

where the operator $\mathcal{L}$ includes unsteady, convection and diffusion terms, while $\mathbf{S}$ represents the TCNE source term. The 10 basic variables are $\boldsymbol{q} = [\rho, u, v, w, T, Y_s, T_v]$ with $s \in [2,5]$. Here ρ is the density; u, v, w the velocities in the streamwise, wall-normal and spanwise/azimuthal directions; $Y_s = \rho_s/\rho$ the species mass fraction of air; T the translational/rotational temperature and T_v the vibrational temperature. A laminar mean flow is needed first for stability analyses. For axisymmetric mean flows, the full N-S equation eq. (1) is solved through a 5th-order shock-fitting solver [13]. A non-catalytic wall boundary condition is assumed for all the species.

2.2 Parabolized stability analyses

The framework of the PSE method is briefly introduced below. The flow variable is decomposed into the steady laminar part $\bar{\boldsymbol{q}}$ and the disturbance part $\widetilde{\boldsymbol{q}}$. The disturbance governing equation is then written as:

$$\mathcal{N}(\bar{\boldsymbol{q}} + \widetilde{\boldsymbol{q}}) - \mathcal{N}(\bar{\boldsymbol{q}}) = \mathbf{S}(\bar{\boldsymbol{q}} + \widetilde{\boldsymbol{q}}) - \mathbf{S}(\bar{\boldsymbol{q}}) \tag{2}$$

The following Fourier decomposition is introduced in the $(x\text{-}y\text{-}\theta)$ coordinates:

$$\widetilde{\boldsymbol{q}} = \sum_{m,n} \hat{\boldsymbol{q}}_{mn} \exp\left[\mathrm{i}\left(\int_{x_0}^{x} \alpha_{mn}\mathrm{d}x + nk_c\theta - m\omega t\right)\right] \tag{3}$$

where $\hat{\boldsymbol{q}}(x,y)$ is the disturbance shape function, k_c and ω the specified azimuthal wavenumber and circular frequency, $\alpha = \alpha_r + \mathrm{i}\alpha_i$ the complex streamwise wavenumber. The notation $(m,\ n)$ is introduced for the disturbance with the frequency of $m\omega$ and azimuthal wavenumber of $n\beta$. Substitute eq. (3) into eq. (2) to obtain the governing equation for each mode. The parabolized form is written as:

$$\hat{\boldsymbol{A}}_{mn}\frac{\partial \hat{\boldsymbol{q}}_{mn}}{\partial x} = -\hat{\boldsymbol{D}}_{mn}\hat{\boldsymbol{q}}_{mn} - \hat{\boldsymbol{B}}_{mn}\frac{\partial \hat{\boldsymbol{q}}_{mn}}{\partial y} + \hat{\boldsymbol{H}}_{mn}\frac{\partial^2 \hat{\boldsymbol{q}}_{mn}}{\partial y^2} + \hat{\boldsymbol{N}}_{mn}\exp\left(-\mathrm{i}\int_{x_0}^{x}\alpha_{mn}\mathrm{d}x\right) \tag{4}$$

where $\hat{\boldsymbol{A}}$, $\hat{\boldsymbol{B}}$, $\hat{\boldsymbol{D}}$, $\hat{\boldsymbol{H}}$ are 10×10 matrix coefficients as the functions of $\bar{\boldsymbol{q}}$, frequency and wavenumbers, and $\hat{\boldsymbol{N}}_{mn}$ is the decomposed nonlinear terms. Equation (4) is for the nonlinear PSE analyses. If the nonlinear term $\hat{\boldsymbol{N}}_{mn}$ is ignored, the equation for each mode is decoupled from each other to give the linear PSE analyses. The non-parallelism of the boundary layer equation is further ignored in LST. One can refer to Ref. [15] for more details.

2.3 Secondary instability analyses

When the two-dimensional/axisymmetric disturbance increases to large amplitudes, the flow profiles distorted by the primary instability disturbance can be again linearly unstable, leading to the rapid growth of three-dimensional waves. The updated basic flow $\bar{\boldsymbol{q}}'$ takes the form as:

$$\bar{\boldsymbol{q}}' = \bar{\boldsymbol{q}} + A_{00}\hat{\boldsymbol{q}}_{00} + \sum_{\substack{m \\ m\neq 0}} A_{m0}\hat{\boldsymbol{q}}_{m0}\exp\left[\mathrm{i}m\left(\alpha_r x - \omega t\right)\right] \tag{5}$$

where A_{mn} is the modal amplitude. The shape functions and wavenumbers of these axisymmetric waves are obtained from the PSE calculations. The governing equation of the secondary disturbance $\widetilde{\boldsymbol{q}}_{\mathrm{sd}}$ is written as:

$$\mathcal{N}\left(\bar{\boldsymbol{q}}' + \widetilde{\boldsymbol{q}}_{\mathrm{sd}}\right) - \mathcal{N}\left(\bar{\boldsymbol{q}}'\right) = \mathbf{S}\left(\bar{\boldsymbol{q}}' + \widetilde{\boldsymbol{q}}_{\mathrm{sd}}\right) - \mathbf{S}\left(\bar{\boldsymbol{q}}'\right) \tag{6}$$

From Floquet theory, the solution takes the form as [5]:

$$\widetilde{\boldsymbol{q}}_{\mathrm{sd}} = \varepsilon\left\{\sum_m \hat{\boldsymbol{q}}_m \exp\left[\mathrm{i}\left(m+\sigma_d\right)\left(\alpha_r x - \omega t\right)\right]\right\}\exp\left(\gamma x + \mathrm{i}k_c\theta\right) \tag{7}$$

Here ε is the wave amplitude and $\gamma = \gamma_r + \mathrm{i}\gamma_i$ is the characteristic exponent, with γ_r the secondary growth rate. The detuning parameter σ_d is introduced to classify different modes: the fundamental resonance is associated with σ_d of 0, while the subharmonic resonance with σ_d of 0.5. The others, at $0 < \sigma_d < 0.5$, are named detuned modes. Substitute eq. (5) and eq. (7) into eq. (6), the governing equation of $\hat{\boldsymbol{q}}_m$ is obtained by further ignoring the terms of $O\left(A^2\right)$, $O\left(\varepsilon^2\right)$ and higher orders. The resulting eigenvalue problem is solved with the same numerical method as that in LST.

3. Simulation setup and linear instability results

The free-stream parameters of the blunt cone flow are shown in table 1, which corresponds to the altitude of 28 km. The nose radius is 4 mm and the cone half-angle is 8°. The wall temperature is set to be 800 K, but the radiative wall boundary condition is used in the head region to allow higher wall temperature due to the extremely high local heat flux [16].

Table 1 – Free-stream conditions for the flow over a blunt cone

Ma_∞	AoA (°)	p_∞ (Pa)	T_∞ (K)	U_∞ (m/s)	Re_∞ (1/m)	$Y_{\mathrm{N}_2,\infty}$
15	0	1616	224.5	4506	7.878×10^6	0.767

The laminar flow field is shown in fig. 1. Due to the high free-stream Mach number, the angle between the far-field shock and the wall is less than 2°. Figure 1(b)∼(d) gives the contours of the temperature, vibration temperature and oxygen mass fraction around the stagnation region. The temperature around the stagnation region exceeds 7000 K but drops rapidly downstream along the wall surface. The vibration energy is continuously excited, and the oxygen near the wall is almost dissociated.
The linear instability characteristics are studied using LST. The neutral curves are calculated first as shown in fig. 2. The growth-rate contours of the axisymmetric ($k_c = 0$) waves are plotted in fig. 2(a).

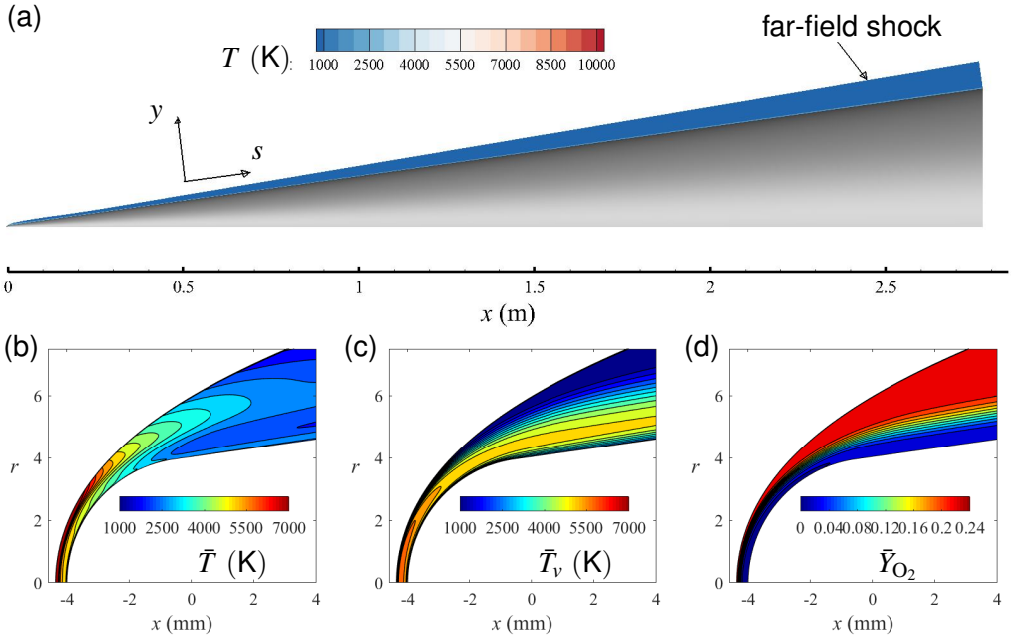

Figure 1 – Contours of the laminar flow: (a) the whole field and (b)∼(d) the head region; (b) temperature, (c) vibrational temperature and (d) oxygen mass fraction

Due to the relatively low wall temperature, the second and third modes are destabilized, while the first mode is stabilized. The frequency range of the second-mode instability region is 280 kHz to 830 kHz within the computational domain. Compared with those of the second mode, the third mode has lower growth rates and higher frequencies. The highest frequency of its unstable wave is as high as 1.15 MHz. It is known that the most unstable Mack modes are two-dimensional, while the dominant first mode is three-dimensional. This trend is in agreement with that in fig. 2(b), where the growth-rate contours of three-dimensional disturbance waves are plotted at $s = 1.4$ m. The first mode instability appears in the azimuthal-wavenumber range of 49 to 119, but its growth rate is much smaller than those of the second and third modes.

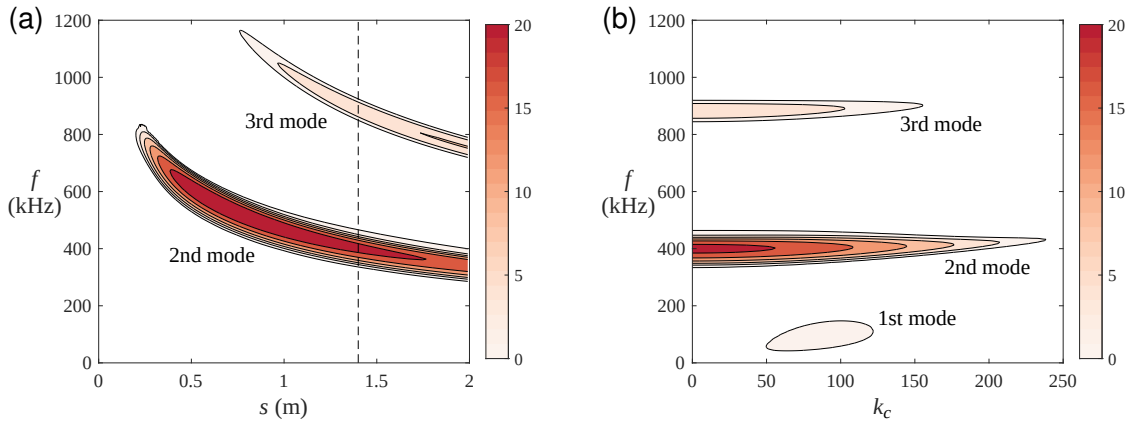

Figure 2 – Growth-rate ($-\alpha_i$, 1/m) contours of the disturbances (a) for axisymmetric waves and (b) with different azimuthal wavenumbers at $s = 1.4$ m

Figure 3 gives a view of the N factor curves, contributed by the axisymmetric second mode, at different frequencies and their envelopes. At the frequency range of 450 kHz to 500 kHz, the maximum N factor of the disturbances is within 8 to 10, and the corresponding streamwise locations are from 1.07 m to 1.3 m. This is the estimated transition onset based on some flight test data [17].

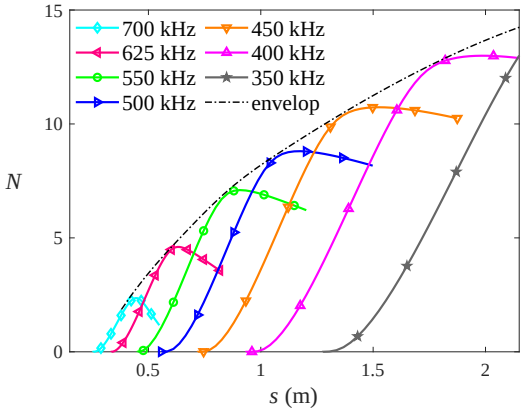

Figure 3 – *N* factor curves of the axisymmetric second-mode waves for the disturbances with different frequencies

4. Fundamental and subharmonic resonance case

This section focuses on the secondary instability process that occurs when the axisymmetric second-mode wave grows to a large amplitude. The two mechanisms studied here are fundamental resonance and subharmonic resonance. Firstly, the axisymmetric second mode (1, 0) is superposed to the laminar flow to see its streamwise evolution. From section 3.the frequency of mode (1, 0) is selected to be 490 kHz, which corresponds to a maximum *N* factor of 9. The initial amplitude is 0.1 %, measured by the temperature disturbance, at the computational inlet s of 0.69 m. The streamwise evolution of mode (1, 0) and its harmonics are depicted in fig. 4(a). The primary wave follows the linear growth downstream until it reaches an amplitude of $O(1)$ at around s of 1.03 m and begins to saturate. Higher-frequency harmonic waves and the mean flow distortion mode (0, 0) show similar curves of the streamwise evolution with rapid amplification and then saturation. Based on the pri-

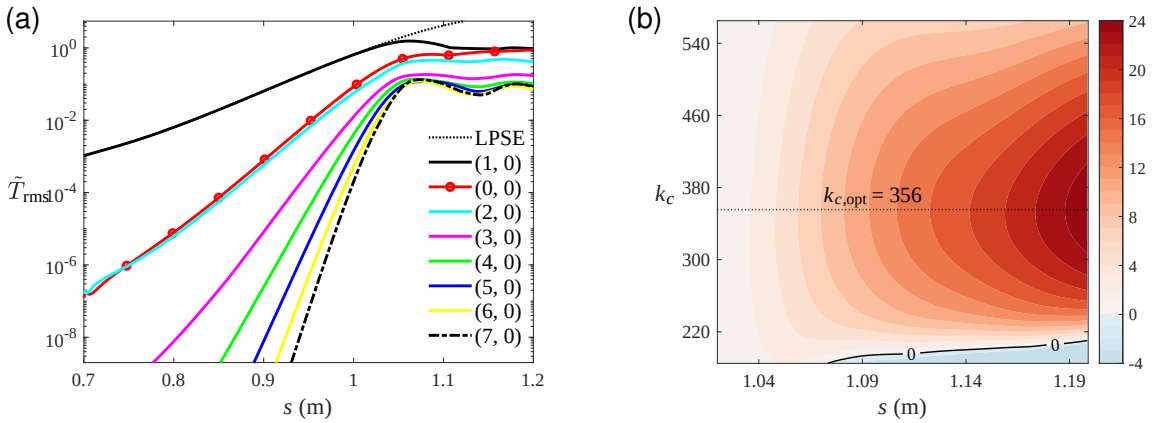

Figure 4 – (a) Streamwise distribution of mode (1, 0) and its harmonics, as well as (b) contours of the secondary *N* factors by SIT of the fundamental mode

mary disturbance flow in fig. 4(a), the growth rates of the fundamental resonance, γ_r (see eq. (7)), are calculated using SIT at different azimuthal wavenumbers. The contours of the *N* factors of the secondary disturbances, N_{sd}, are drawn in fig. 4(b) with the starting point at $s = 1.02$ m. The optimal azimuthal wavenumber $k_{c,opt}$, at which the secondary disturbance experiences the strongest growth, is measured to be 356 under the current computational parameters. The growth rates of the subharmonic resonance are also calculated at $s = 1.1$ m, as is shown in fig. 5(a). It is shown that the subharmonic resonance has much lower growth rates than those of the fundamental resonance. Also, the azimuthal wavenumber corresponding to the maximum growth rate is smaller in the subharmonic resonance case.

For verification, the NPSE calculation is performed with initial mode (1/2, 1) at k_c of 200. As is shown

in fig. 5(b), mode (1/2, 1) experiences the subharmonic growth with the saturation of mode (1, 0). However, the growth rate is relatively low, and the amplitude is only increased by 10 times at 1.2 m. In contrast, mode (1, 2), generated by mode (1/2, 1) through nonlinear interactions, experiences rapid growth through the fundamental resonance with mode (1, 0) at k_c of 400. Although the initial amplitude of mode (1, 2) is only 10^{-12}, its amplitude is equivalent to mode (1, 0) at $s = 1.2$ m. The phase velocity curves indicate that mode (1, 2) is phase-locked with mode (1, 0) in the resonance region. This phase-locking state provides the optimal chance of the energy transfer from the primary wave to the secondary [18]. In contrast, mode (1/2, 1) is phase-detuned with mode (1, 0), and the phase difference between the two is alternately positive and negative. The resulting growth rate is thus much lower in the subharmonic resonance.

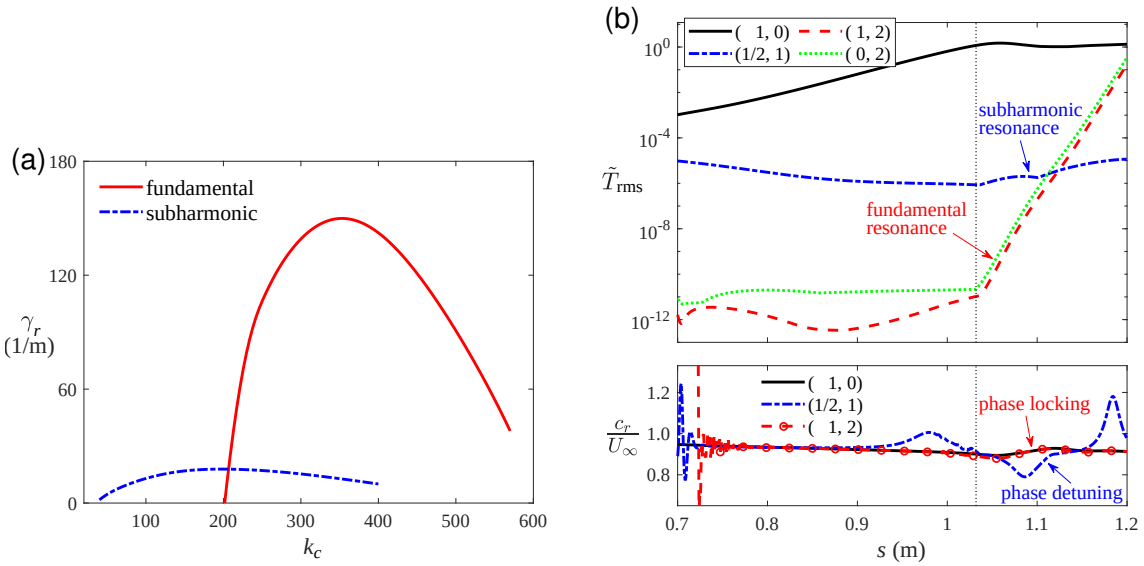

Figure 5 – (a) Growth rate by SIT of the fundamental and subharmonic modes with different azimuthal wavenumbers at $s = 1.1$ m, and (b) streamwise distribution of the amplitudes and phase speeds of representative modes in the subharmonic resonance case

5. Oblique-mode breakdown case

Compared with the fundamental and subharmonic resonance, the oblique-mode breakdown case only contains a pair of oblique second-mode waves (1,±1) at the inlet. The frequency of the second mode is also 490 kHz, and the azimuthal wavenumber is selected to be $k_c = 40$. Figure 6(a) gives the streamwise evolution of the amplitudes of typical modes. At $s = 1.04$ m, mode (1, 1) starts to deviate from the linear trajectory towards saturation. The streamwise-vortex mode (0, 2) grows stronger than mode (2, 0), and its amplitude exceeds mode (1, 1) downstream s of 1.10 m. Also, the other streamwise-vortex modes, (0, 4), (0, 6), etc., all grow to the amplitudes of $O(1)$ in the saturation region. Moreover, the amplitudes of the modes with the same frequency and different azimuthal wavenumbers are close to each other in the saturation zone and gradually decrease with the increase in frequency. Therefore, the steady streamwise-vortex modes dominate the flow in the early transitional region. Figure 6(b) gives the streamwise evolution of the Reynolds-averaged wall-friction coefficient C_f. In the NPSE calculation, C_f has 5 % deviation from the laminar value at $s = 1.08$ m, which is defined as the transition onset in this paper. With the growth of the streamwise-vortex and harmonic modes, C_f continuously grows to exceeds two times of the laminar counterpart.

6. Effects of thermal-chemical non-equilibrium

For comparison, the cases in the above sections are also calculated within the CPG assumption. To control variables, the transport model in section 2.1is used, instead of Sutherland's law, in the CPG calculations. The laminar temperature profiles are first compared at two streamwise locations in fig. 7(a)&(b). The differences in the maximum temperatures decreases from 450 K at $s = 0.15$ m

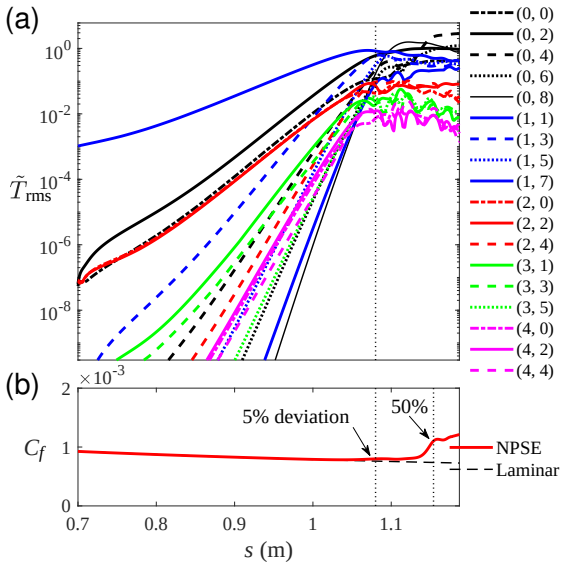

Figure 6 – Streamwise development of (a) the amplitude of typical modes and (b) the Reynolds-averaged wall-friction coeffcient in the oblique breakdown case

to 120 K at 1 m. The influence of TCNE on the linear instabilities mainly comes from the change in the laminar flow profiles under the current physical models [19]. As a result, the cooler and thinner boundary layers in TCNE flows destabilize the second mode and moves upstream the N-factor envelope by around 0.1 m for axisymmetric disturbances, as is shown in fig. 7(c). The growth rates of

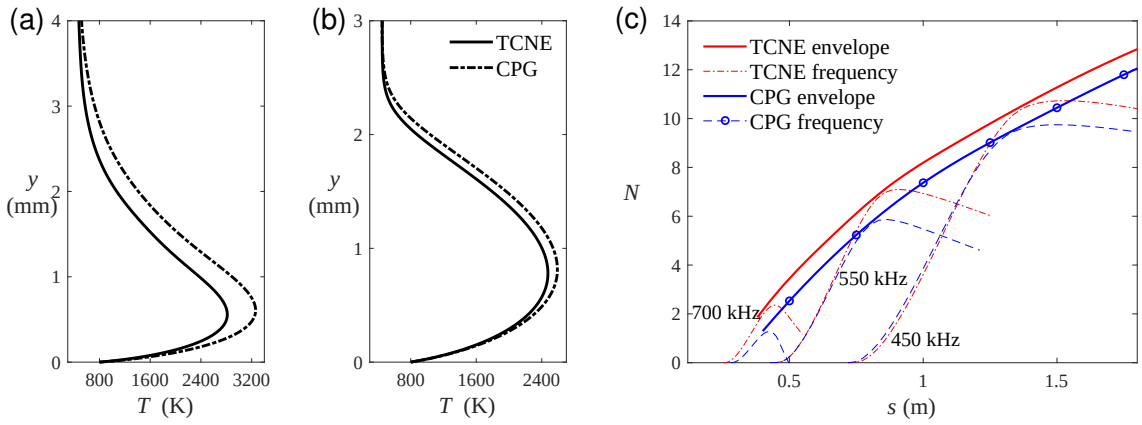

Figure 7 – Laminar temperature profiles at (a) $s = 0.15$ m, (b) $s = 1$ m, as well as (c) the N factor curves for the TCNE and CPG cases

the fundamental resonance are compared in fig. 8 with the amplitude of the second-mode at 1 and 2, respectively. The growth rate and the azimuthal wavenumber corresponding to the most unstable wave are both larger in TCNE flows. For the oblique-mode breakdown case, the higher growth rate of the second-mode waves leads to faster growth of the streamwise vortex and other harmonic waves.

7. Conclusion

In this paper, the NPSE and SIT methods are used to study the two most important transition mechanisms, the secondary instability of the axisymmetric second-mode wave and the second-mode oblique-wave breakdown, in the hypersonic and high-enthalpy boundary layers with thermal-chemical non-equilibrium effects. The case studied is the flow over a blunt cone with the free-stream Mach-number of 15 and zero angle-of-attack. In the fundamental resonance, the three-dimensional disturbances are phase-locked with the primary axisymmetric waves, leading to the rapid growth of the oblique and streamwise-vortex waves. In contrast, the three-dimensional waves are phase-detuned

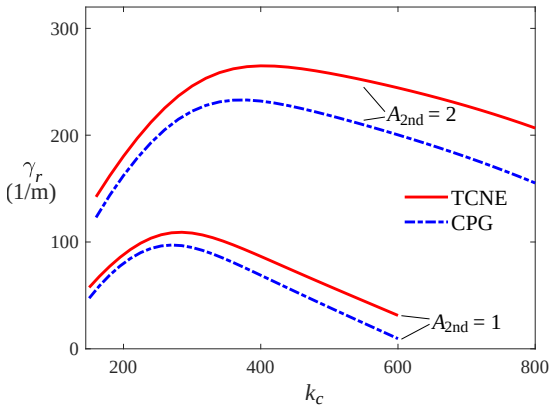

Figure 8 – Growth rates of the fundamental mode for the CPG and TCNE cases with different amplitudes of the primary second-mode waves

in the subharmonic resonance, and the secondary growth rate is relatively low. Therefore, the fundamental resonance is found to dominate over the subharmonic resonance. Taking advantage of the high efficiency of SIT, the optimal azimuthal wavenumber is determined corresponding to the strongest secondary growth. For the oblique-mode breakdown case, the steady streamwise-vortex modes have the largest amplitude in the saturation region compared to the unsteady modes. Large-amplitude streamwise vortices lead to the rapid exchange of momentum, energy and mass between fluid layers with different wall-normal heights. For the fundamental resonance, the effects of TCNE on the secondary instability are found similar to increase the primary wave amplitude that leads to a higher maximum secondary growth rate and the corresponding azimuthal wavenumber. For the oblique-mode breakdown, the higher growth rate of the second-mode waves leads to faster growth of the streamwise vortex and other harmonic waves.

Contact Author Email Address

Mail-to: fs-dem@tsinghua.edu.cn

Copyright Statement

References

[1] M. V. Morkovin. Transition at hypersonic speeds. Technical report, NASA Langley Research Center, 1987.

[2] J. D. Anderson Jr. *Hypersonic and high-temperature gas dynamics, second edition*. AIAA, 2006.

[3] E. Reshotko. Transition issues for atmospheric entry. *Journal of Spacecraft and Rockets*, 45(2):161–164, 2008.

[4] L. M. Mack. *Boundary-layer linear stability theory*. 1984.

[5] T. Herbert. Secondary instability of boundary layers. *Annual Review of Fluid Mechanics*, 20:487–526, 1988.

[6] K. J. Franko and S. K. Lele. Breakdown mechanisms and heat transfer overshoot in hypersonic zero pressure gradient boundary layers. *Journal of Fluid Mechanics*, 730:491–532, 2013.

[7] C. D. Pruett and C.-L. Chang. Spatial direct numerical simulation of high-speed boundary-layer flows part II: transition on a cone in Mach 8 flow. *Theoretical & Computational Fluid Dynamics*, 7(5):397–424, 1995.

[8] J. Sivasubramanian and H. F. Fasel. Direct numerical simulation of transition in a sharp cone boundary layer at Mach 6: fundamental breakdown. *Journal of Fluid Mechanics*, 768:175–218, 2015.

[9] X. Chen, Y. Zhu, and C. Lee. Interactions between second mode and low-frequency waves in a hypersonic boundary layer. *Journal of Fluid Mechanics*, 820:693–735, 2017.

[10] P. A. Gnoffo, R. N. Gupta, and J. L. Shinn. Conservation equations and physical models for hypersonic air flows in thermal and chemical nonequilibrium. Technical report, NASA Langley Research Center, 1989.

[11] H. B. Johnson, T. G. Seipp, and G. V. Candler. Numerical study of hypersonic reacting boundary layer transition on cones. *Physics of Fluids*, 10(10):2676–2685, 1998.

[12] O. Marxen, G. Iaccarino, and T. E. Magin. Direct numerical simulations of hypersonic boundary-layer transition with finite-rate chemistry. *Journal of Fluid Mechanics*, 755:35–49, 2014.

[13] X. Chen and S. Fu. Convergence acceleration for high-order shock-fitting methods in hypersonic flow applications with efficient implicit time-stepping schemes. *Computers & Fluids*, 210:104668, 2020.

[14] X. Chen, L. Wang, and S. Fu. Parabolized stability analysis of hypersonic thermal-chemical nonequilibrium boundary-layer flows. *AIAA Journal*, 59(7):2382–2395, 2021.

[15] C.-L. Chang. Langley stability and transition analysis code (LASTRAC) version 1.2 user manual. Technical report, NASA Langley Research Center, 2004.

[16] C. H. Mortensen. Toward an understanding of supersonic modes in boundary-layer transition for hypersonic flow over blunt cones. *Journal of Fluid Mechanics*, 846:789–814, 2018.

[17] M. R. Malik. Hypersonic flight transition data analysis using parabolized stability equations with chemistry effects. *Journal of Spacecraft & Rockets*, 40(3):332–344, 2003.

[18] X. Wu and P. A. Stewart. Interaction of phase-locked modes: a new mechanism for the rapid growth of three-dimensional disturbances. *Journal of Fluid Mechanics*, 316:335–372, 1996.

[19] N. P. Bitter. *Stability of hypervelocity boundary layers*. PhD thesis, California Institute of Technology, 2015.